electronics

MDPI

Article

3D-Printed Turnstile Junction Orthomode Transducers: Design, Fabrication, and Measurements

Keyi Ma, Xin Wen, John S. Kot and Rodica Ramer *

School of Electrical Engineering and Telecommunications, The University of New South Wales Sydney, Sydney, NSW 2052, Australia; keyi.ma@unsw.edu.au (K.M.); xin.wen9@unsw.edu.au (X.W.); john.kot@yker.com.au (J.S.K.)
* Correspondence: ror@unsw.edu.au

Abstract

Orthomode transducers (OMTs) are critical for communications, enabling frequency reuse through orthogonal polarization separation, yet traditional manufacturing faces challenges in cost, weight, and complexity at high frequencies. This study explores additive manufacturing (AM) for fabricating high-performance OMTs for X-band and Ka-band applications. Two turnstile-junction-based OMTs were designed, optimizing a symmetrical architecture for low return loss, high isolation, and broadband operation. Both OMTs were fabricated using 3D printing technologies, with a comparative analysis of different AM techniques on performance. Measurements validated simulation results, achieving good return loss for both OMTs and isolation above 35 dB for the X-band and above 25 dB for the Ka-band. These designs meet the requirements of modern communication antenna feed systems across multiple frequency bands. Additionally, 3D printing demonstrates the promising potential of AM in RF component manufacturing, offering performance comparable to traditional metal-machined parts.

Keywords: orthomode transducer; additive manufacturing; turnstile junction; satellite communications

check for updates

Academic Editors: Sensong An and Bowen Zheng

Received: 19 September 2025
Revised: 10 October 2025
Accepted: 14 October 2025
Published: 16 October 2025

Citation: Ma, K.; Wen, X.; Kot, J.S.; Ramer, R. 3D-Printed Turnstile Junction Orthomode Transducers: Design, Fabrication, and Measurements. *Electronics* **2025**, *14*, 4074. https://doi.org/10.3390/electronics14204074

Copyright: © 2025 by the authors. Licensee MDPI, Basel, Switzerland. This article is an open access article distributed under the terms and conditions of the Creative Commons Attribution (CC BY) license (https://creativecommons.org/licenses/by/4.0/).

1. Introduction

Orthomode transducers (OMTs) are essential components in modern microwave and radiofrequency (RF) systems, particularly in modern communication systems, where they enable frequency reuse by separating or combining orthogonal linear polarizations (LP) [1–4]. In circular polarization (CP) systems, an OMT plays a critical role in mitigating mismatches that generate unwanted cross-polarized fields, thereby improving axial ratio (AR) performance and facilitating accurate AR measurements [5–8]. Some OMTs can employ higher-order-mode OMTs to realize multiplexing of multiple polarizations and modes within the same waveguide, thereby enhancing spectral efficiency [9,10]. Traditional OMT designs, such as those based on turnstile junctions or septum structures, have been fabricated using subtractive manufacturing techniques like CNC milling. While this approach offers excellent precision, it is associated with high costs and long production times. By contrast, additive manufacturing (AM) provides unique advantages in terms of flexibility, reduced weight, rapid prototyping, and cost-effective production of complex structures, making it an attractive alternative for RF component fabrication [11–13].

The demand for compact, lightweight, and broadband OMTs has intensified with the evolution of different communication bands, including X-band and Ka-band, which require devices capable of handling wide bandwidths while maintaining low return loss

and high isolation [14,15]. At these frequencies, traditional metal-machined OMTs become increasingly expensive, with assembly complexities and sensitivity to fabrication tolerances. Additive manufacturing (AM), emerges as a transformative solution, enabling rapid prototyping, reduced weight, and cost-effective production of intricate waveguide structures [16–18]. Technologies such as stereolithography (SLA), selective laser sintering (SLS), and selective laser melting (SLM) allow for the fabrication of polymer- or metal-based components with micro-level precision, making them suitable for micro-scale RF devices [19–21]. However, AM introduces challenges like surface roughness, material conductivity, and dimensional accuracy, which can impact RF performance, necessitating comparative studies to optimize fabrication parameters [22,23].

This work presents the design, simulation, fabrication, and experimental validation of two turnstile-junction-based OMTs designed to operate in a communication system application, leveraging AM to achieve compact, high-performance devices. The symmetrical turnstile architecture is selected for its inherent broadband isolation and mode separation capabilities, outperforming asymmetrical septum designs in polarization purity [24–26]. In this work, the impact of fabrication tolerances on this architecture is explicitly examined, with measured dimensional errors and their effects on device performance reported in Section 4. The first OMT targets the X-band, while the second extends to the Ka-band, demonstrating scalability to higher frequencies with enhanced bandwidth. Both designs incorporate a circular waveguide input for dual-polarized signals and rectangular waveguide outputs, optimized using CST Microwave Studio 2023 for key parameters.

Fabrication is performed using SLA with photocurable resins for low-cost prototypes, followed by conductive silver painting and copper electroplating to enhance conductivity. A comparative study includes an SLM-fabricated aluminum version to evaluate the influence of printing technology and material on performance metrics. Measurements using a vector network analyzer (VNA) confirm alignment with simulations, achieving return losses > 20 dB, isolation > 35 dB, and low insertion losses, while highlighting trade-offs in precision.

The novelty of this research lies in the application of AM to high-performance waveguide OMTs from X- to Ka-band while maintaining broadband operation. This approach demonstrates AM's viability for RF micromachining and paves the way for future applications in 5G/6G communications, satellite ground and space segments, radar systems, and AR measurement. The following sections detail the design methodology, simulation results, fabrication processes, and comparative analysis, concluding with prospects for higher-frequency extensions.

2. Detailed Design of Orthomode Transducer

The design of the proposed OMTs was determined by three main objectives: broadband isolation, acceptable insertion loss, and rapid fabrication using additive manufacturing techniques. Symmetrical turnstile junction architecture was selected as the core structure because it can provide good mode separation and wideband isolation, ensuring high polarization purity across the operating bands [27]. The design process was finished in CST Microwave Studio using a combination of parametric sweeps and optimizers. Key parameters such as the radius and height of the cone-shaped divider and the thickness of the impedance-matching steps in the T-junctions were iteratively tuned to minimize return loss and maximize isolation across the target frequency ranges.

Several challenges were encountered during the design stage. Achieving wideband matching at higher frequencies requires precise optimization of the circular-to-rectangular transitions, while maintaining structural symmetry is critical to ensure high isolation. In addition, the geometry can be changed to comply with the dimensional limits and

resolution of SLA and SLM fabrication processes. Considering fabrication errors, tolerance effects were incorporated into the design analysis. Although the CST simulations were based on idealized geometries, additional simulations were performed by introducing the maximum dimensional deviations expected from the 3D printing process. These studies can be used to evaluate the influence of size variations on key performance parameters such as return loss, insertion loss, and isolation. The impact of fabrication tolerances is further examined in Section 4, where measured dimensional errors are reported and their correlation with RF performance is analyzed.

2.1. Turnstile Junction

The turnstile junction serves as the core component of the OMT, functioning as a polarization duplexer to separate or combine two orthogonally polarized signals within a single circular waveguide port into or from two distinct rectangular waveguide ports. The turnstile junction operates as a six-port network, comprising one circular waveguide port supporting two orthogonal TE_{11} modes and four rectangular waveguide ports, each supporting a single TE_{10} mode, resulting in six electrical ports, as shown in Figure 1. The equivalent circuit is depicted in Figure 2, where a_n^- and a_n^+ represent the incident and reflected wave amplitudes at the nth port. The ideal scattering matrix for this network is derived based on matching, isolation, and the properties of symmetrical, reciprocal networks, as shown in (1). Due to the junction's inherent symmetry, many scattering matrix entries are identical or have equal magnitude but opposite signs. For instance, when power splits equally between two ports, the scattering parameters are $1/\sqrt{2}$ or $-1/\sqrt{2}$, reflecting power proportionality to voltage squared. Zero diagonal entries indicate matched ports with no reflection, while off-diagonal zeros correspond to ports isolated by symmetry.

$$\begin{pmatrix} a_1^- \\ a_2^- \\ a_3^- \\ a_4^- \\ a_5^- \\ a_6^- \end{pmatrix} = \begin{pmatrix} \frac{1}{2} & 0 & -\frac{1}{2} & 0 & \frac{1}{\sqrt{2}} & 0 \\ 0 & \frac{1}{2} & 0 & -\frac{1}{2} & 0 & \frac{1}{\sqrt{2}} \\ -\frac{1}{2} & 0 & \frac{1}{2} & 0 & \frac{1}{\sqrt{2}} & 0 \\ 0 & -\frac{1}{2} & 0 & \frac{1}{2} & 0 & \frac{1}{\sqrt{2}} \\ \frac{1}{\sqrt{2}} & 0 & \frac{1}{\sqrt{2}} & 0 & 0 & 0 \\ 0 & \frac{1}{\sqrt{2}} & 0 & \frac{1}{\sqrt{2}} & 0 & 0 \end{pmatrix} \begin{pmatrix} a_1^+ \\ a_2^+ \\ a_3^+ \\ a_4^+ \\ a_5^+ \\ a_6^+ \end{pmatrix} \quad (1)$$

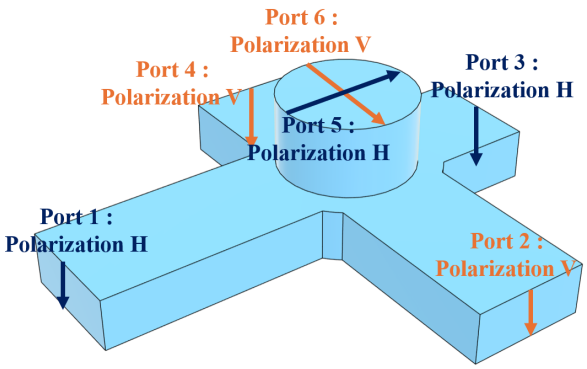


Figure 1. Overview of the six electrical ports of the proposed turnstile junction.

For example, exciting port 5 (one TE_{11} mode in the circular waveguide) results in a perfectly matched port ($S_{55} = 0$), with the signal splitting equally between rectangular ports 1 and 3 (S_{51} and S_{53} with magnitude $1/\sqrt{2}$). Due to the opposite directions of the H-fields in the TE_{11} and TE_{10} modes, these parameters have opposite signs. Ports 2 and 4, whose E-fields are orthogonal to the TE_{11} mode, exhibit no coupling ($S_{52} = S_{54} = 0$). Symmetry dictates the scattering parameters for port 6 (the other TE_{11} mode), while odd and even

symmetry excitations determine the diagonal entries for rectangular waveguide modes. The reciprocal nature of the network ensures $S_{mn} = S_{nm}$, completing the matrix. In practice, real junctions yield frequency-dependent approximations of these ideal values.

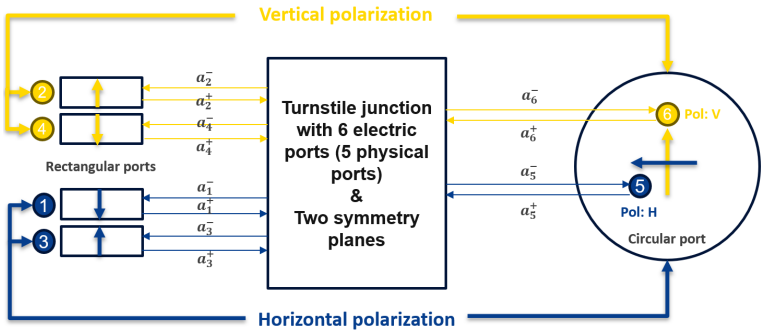


Figure 2. Equivalent circuit of the proposed turnstile junction.

To highlight the turnstile junction's symmetry, the ports can be renumbered to produce the scattering matrix in (2), revealing two independent electrical networks due to the structure's two symmetrical planes, which ensure high isolation.

$$\begin{pmatrix} a_1^- \\ a_3^- \\ a_5^- \\ a_2^- \\ a_4^- \\ a_6^- \end{pmatrix} = \begin{pmatrix} \frac{1}{2} & -\frac{1}{2} & \frac{1}{\sqrt{2}} & 0 & 0 & 0 \\ -\frac{1}{2} & \frac{1}{2} & \frac{1}{\sqrt{2}} & 0 & 0 & 0 \\ \frac{1}{\sqrt{2}} & \frac{1}{\sqrt{2}} & 0 & 0 & 0 & 0 \\ 0 & 0 & 0 & \frac{1}{2} & -\frac{1}{2} & \frac{1}{\sqrt{2}} \\ 0 & 0 & 0 & -\frac{1}{2} & \frac{1}{2} & \frac{1}{\sqrt{2}} \\ 0 & 0 & 0 & \frac{1}{\sqrt{2}} & \frac{1}{\sqrt{2}} & 0 \end{pmatrix} \begin{pmatrix} a_1^+ \\ a_3^+ \\ a_5^+ \\ a_2^+ \\ a_4^+ \\ a_6^+ \end{pmatrix} \quad (2)$$

The design of the OMT is based on the symmetry expressed in (2), which gives a high degree of isolation between the two orthogonal polarizations. The main design goal is to match the circular-to-rectangular waveguide junctions over the desired frequency band. This is achieved with the cone-shaped matching structure shown in Figure 3, with the dimensions optimized in CST. To complete the design, each pair of rectangular waveguides connected to the turnstile junction is combined into a single rectangular waveguide port. This is done using phase-matched waveguide networks comprising 90-degree waveguide bends, and E-plane tee junctions, which are described in the following sections.

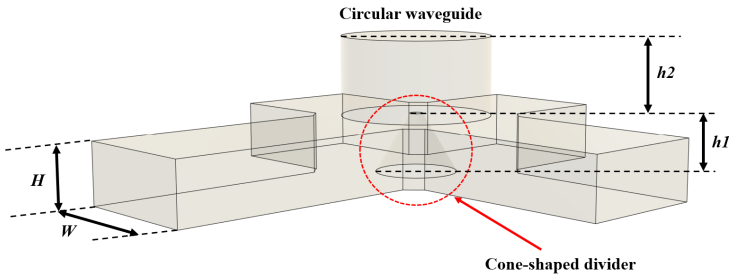


Figure 3. Turnstile structure with circular and rectangular waveguides.

For the X-band OMT, the circular waveguide radius was set to 16.55 mm to match an existing polarizer, paired with WR112 rectangular waveguides. For the Ka-band OMT, the radius was reduced to 4.75 mm, with WR28 waveguides. Figure 3 shows the specific structure of the turnstile junction. The main parts include four standard rectangular waveguides of the same size and one circular waveguide. The size of the circular waveguide is determined by the antenna feed network it is adapted to. To create a wideband match

between the rectangular waveguide network and the circular waveguide port, a cone-shaped structure divider is added at the bottom of the turnstile junction. In Figure 3, *H* and *W* are the height and width of the standard rectangular waveguide used, respectively. *h1* is the height of the conical divider, and *h2* is the length of the circular waveguide. Figure 4a shows the top view of the turnstile junction. The radius of the circular waveguide is *R1*, and the radius of the virtual circle used for the circular arc transition is *R2*. The lengths of the four rectangular waveguides are *L1*, *L2*, *L3*, and *L4*. Figure 4b shows the bottom view of the turnstile junction. The diameters of the bottom and top circles of the conical structure in Figure 4b are *D1* and *D2*.

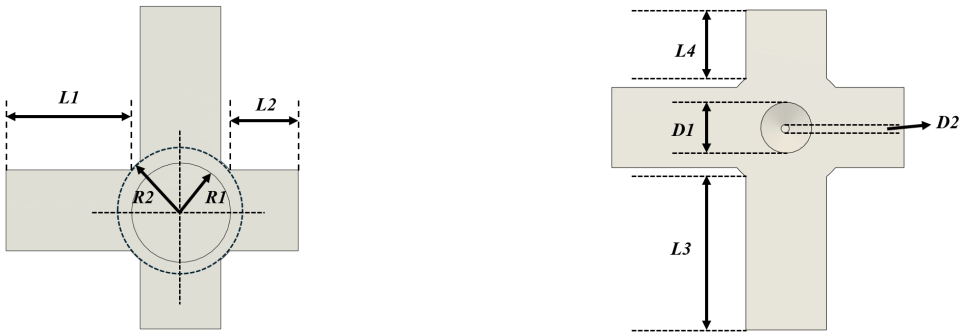


Figure 4. Top and bottom views of the turnstile junction. (**a**) Top view; (**b**) bottom view.

2.2. 90° E-Plane Waveguide Bend

The 90° E-plane waveguide bends connect the turnstile junction's rectangular ports to the T-junction, redirecting the signal path while minimizing reflections. A radiused bend design was employed, with the radius set to exceed two wavelengths to reduce continuous reflection due to curvature. The bend geometry was optimized to ensure that reflections at the interfaces between straight and curved waveguide sections are 180° out of phase. Figure 5 shows two different 90° E-plane bent waveguides. The bent part is a quarter-sector annular waveguide. The inner radius of the annular ring is *Rc1*, and the outer radius is *Rc2*. Each bent waveguide consists of two identical sectoral annular waveguides, which are connected by rectangular waveguides of different lengths. The length of the rectangular waveguide in the first bent waveguide is *h3*, and the length of the second one is *h4*. The OMT includes two E-plane waveguide bends to connect the turnstile junction to the T-junction.

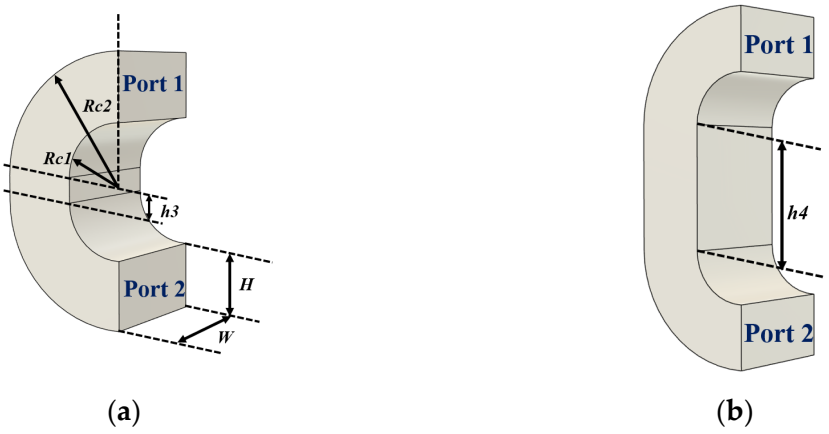


Figure 5. Two 90° E-plane waveguide bends. (**a**) First 90° E-plane waveguide bend; (**b**) second 90° E-plane waveguide bend.

2.3. T-Junction

The T-junction combines signals from two symmetrical rectangular waveguides into a single output port. The triangular protrusion at the center of the junction redirects electromagnetic waves by 90° and, combined with the quarter-wavelength impedance matching stepped structure, minimizes reflections. The number and thickness of these stepped structures were optimized in CST to achieve phase cancelation of the reflected waves. The Ka-band T-junction follows the same design principles, with smaller dimensions and exhibiting comparable performance. Figure 6 shows the main structure of the T-junction. The bottom waveguide of the T-junction serves as an input port for one mode and contains sectoral annular waveguides and rectangular waveguides of the same size as the E-plane waveguide bend. The lengths of the rectangular waveguides are *L5* and *h5*. The lengths of the rectangular waveguides used to connect to the two E-plane waveguide bends are *L6* and *L7*. Figure 7 shows the details of the stepped structure. The stepped structures are symmetrical left and right, and each contains two steps. Each step has a length of *l1* and a height of *l2*. To eliminate reflections at the connection, a triangular-shaped transition was used. Each triangle has a hypotenuse length of *l3* and is at a 45° angle to the plane. The OMT contains a total of two stepped T-junctions.

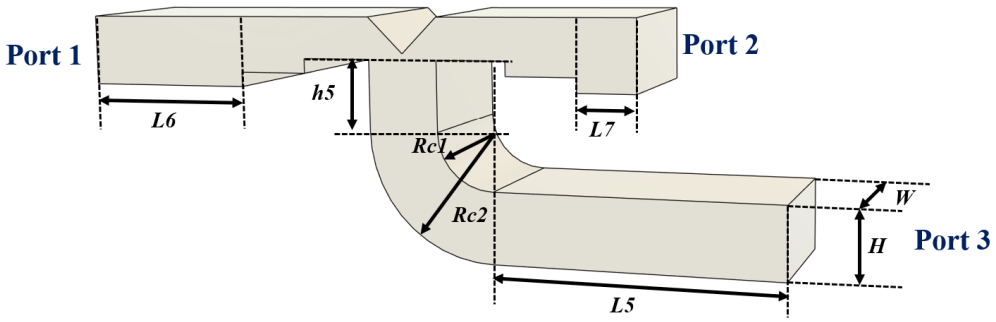


Figure 6. Stepped T-junction structure.

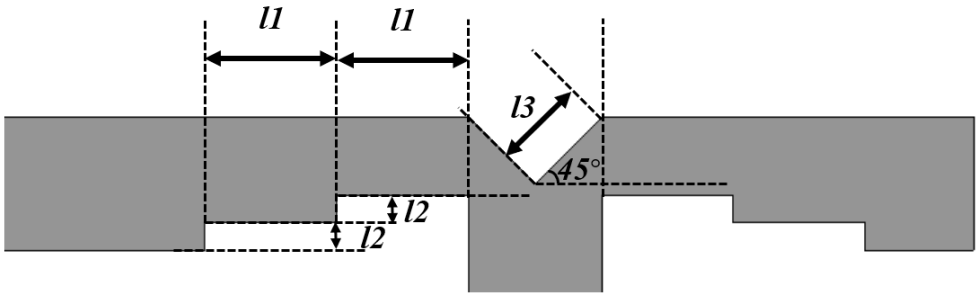


Figure 7. Front view of a detailed stepped structure in a T-junction.

2.4. Entire Orthomode Transducer

The complete OMT integrates the Turnstile junction, E-plane bends, and T-junctions into two independent rectangular waveguide networks, one for each polarization. This design ensures that the path lengths are nearly identical, which maintains performance symmetry. Figure 8 shows the complete OMT design. At the very top of the OMT is a Turnstile junction, where its four rectangular waveguides connect to two different E-plane waveguide bends. Each pair of waveguide bends then connects to a T-junction. The parameters for the OMT vary for different frequency bands. Tables 1 and 2 show the OMT design parameters for various frequency bands, respectively.

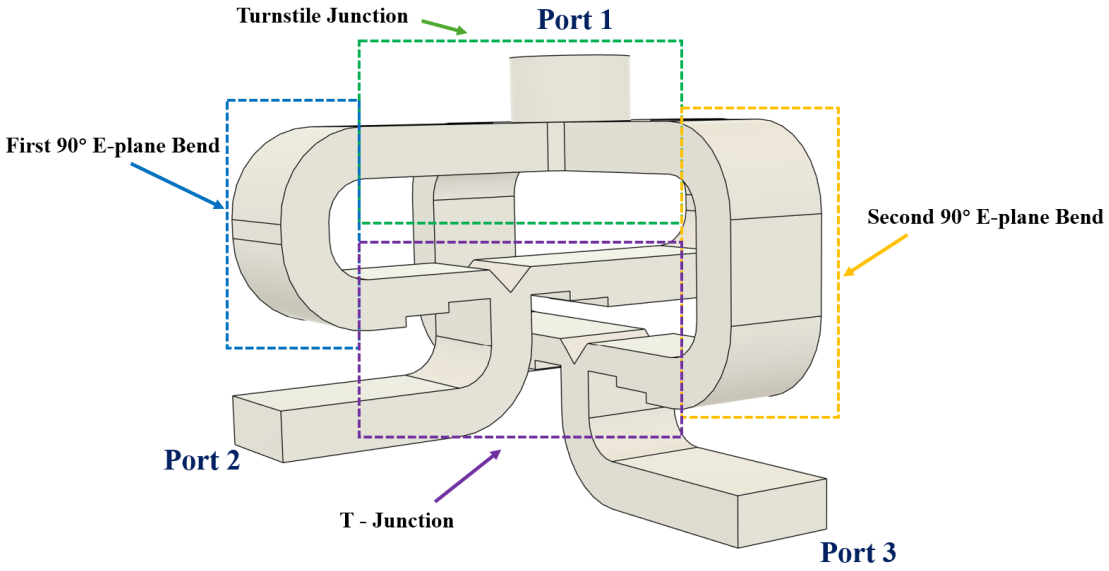


Figure 8. Entire OMT structure.

Table 1. Values of parameters of X-band OMT.

Parameter	Value (mm)	Parameter	Value (mm)	Parameter	Value (mm)
H	12.6238	*h1*	13	*L4*	54.2
W	28.4988	*h2*	17.4	*L5*	50
R1	16.5	*h3*	4.76	*L6*	30.3
R2	22.6	*h4*	24.75	*L7*	10.3
D1	18	*h5*	12.58	*l1*	12.5
D2	3	*L1*	44.2	*l2*	2.6
Rc1	10	*L2*	24.2	*l3*	9
Rc2	22.62	*L3*	24.2		

Table 2. Values of parameters of Ka-band OMT.

Parameter	Value (mm)	Parameter	Value (mm)	Parameter	Value (mm)
H	3.556	*h1*	2.8	*L4*	13.13
W	7.112	*h2*	5.25	*L5*	12.5
R1	4.75	*h3*	0.38	*L6*	6.02
R2	5.63	*h4*	5.38	*L7*	1.55
D1	3	*h5*	5.34	*l1*	3.1
D2	0.5	*L1*	9.63	*l2*	0.7
Rc1	2.5	*L2*	4.63	*l3*	2.6
Rc2	6.056	*L3*	5.63		

3. Simulation Results

3.1. X-Band Orthomode Transducer

Based on the detailed design of each component, the X-band OMT was first simulated in CST Microwave Studio, starting with the turnstile junction. Figure 9 presents the simulation results. It can be observed that the return loss at the circular waveguide port is below −20 dB across the entire frequency band, indicating excellent matching performance. As the wave at the circular waveguide port is divided into two parts, each rectangular waveguide port exhibits an insertion loss of −3 dB, demonstrating that the simulated turnstile junction achieves a high coupling level, consistent with theoretical calculations.

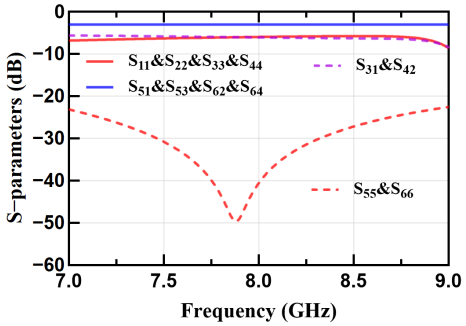


Figure 9. Simulated turnstile junction results.

The simulated results of the 90° E-plane waveguide bend are shown in Figure 10. The return loss at both the input and output ports of the two waveguides is below −30 dB, indicating excellent matching performance. Additionally, the transmission coefficient at both ports is nearly 0 dB, meaning the simulated E−plane bend structure has almost no insertion loss, ensuring a high transmission level.

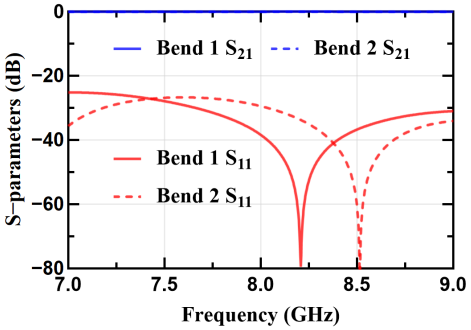


Figure 10. Simulated 90° E−plane waveguide bends and results.

The simulated results of the T-junction are shown in Figure 11. It can be observed that the return loss at the merged port is below −20 dB across the entire frequency band, indicating excellent matching performance. Additionally, as the two waves combine into one, each port on the left and right arms exhibits an insertion loss of −3 dB, demonstrating that the simulated T-junction achieves a high coupling level, consistent with theoretical expectations.

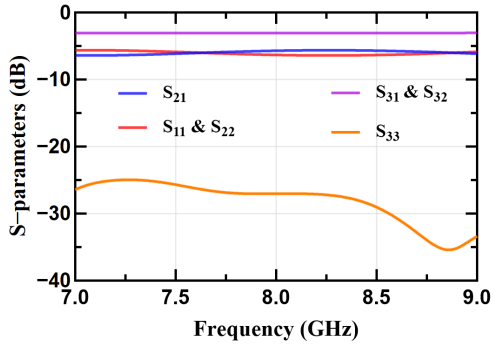


Figure 11. Simulated T−junction results.

Figure 12 shows the simulation results of the combined OMT. The return loss at all three ports is below −20 dB, indicating excellent matching performance at each port. Additionally, the transmission coefficient of the two output ports is nearly 0 dB, confirming the feasibility of each transmission network. Moreover, the isolation between the two output ports is below −60 dB, demonstrating the symmetry and orthogonal separation

capability of the proposed OMT. The sharp peaks observed in the simulated results around 7.6–7.8 GHz are caused by very low-level coupling to higher-order modes in the idealized OMT model. In the real structure, finite conductivity of the metallized surfaces, surface roughness, and assembly imperfections suppress these resonances, and therefore, they are not present in the measured results.

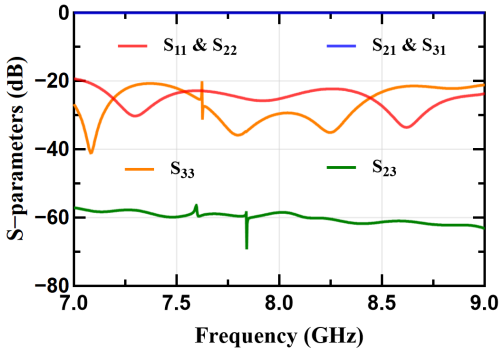


Figure 12. Simulated whole 3−port X−band OMT S−parameter results.

3.2. Ka Band Orthomode Transducer

Similarly to the X-band OMT, the Ka-band OMT is also simulated based on CST, utilizing the same procedures and processes. Figure 13 indicates the simulated results of Ka-band OMT. The Ka-band OMT achieved similar results, with return losses below −20 dB at three ports, transmission coefficients near 0 dB, and isolation below −60 dB across the 26.5–38 GHz band. These results highlight the design's robustness across frequency bands and its ability to eliminate reflected waves, making it suitable for axial ratio measurements in CP systems. The simulations validated the theoretical design, demonstrating that the turnstile-based OMT achieves high isolation, low insertion loss, and broadband performance. The use of CST's built-in optimizer facilitated parametric studies, adjusting critical dimensions such as the turnstile junction's cone-shaped distributor, E-plane bend curvature, and T-junction ladder configurations to achieve optimal S-parameters. These simulations provided a solid foundation for fabrication, ensuring that the designs are both theoretically sound and practically realizable using additive manufacturing techniques.

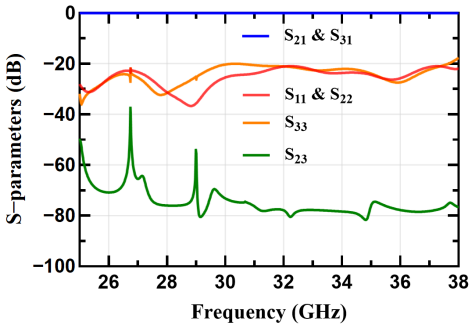


Figure 13. Simulated whole 3−port Ka band OMT S-parameter results.

3.3. Design Tolerance Analysis

Figures 14 and 15 present the tolerance analysis results for the X-band and Ka-band OMTs under ±400 µm dimensional deviations. For the X-band case, the return loss remains below 15 dB across the band, while insertion loss gradually increases and isolation begins to degrade beyond 300 µm due to loss of structural symmetry. In contrast, the Ka-band OMT exhibits higher sensitivity to tolerances. 400 µm deviations lead to noticeable degradation in return loss and transmission, with isolation decreasing. Nevertheless, the isolation

performance remains within an acceptable range for practical application. The results confirm that the performance of both OMTs maintains good stability against dimensional changes, showing a high tolerance to manufacturing errors.

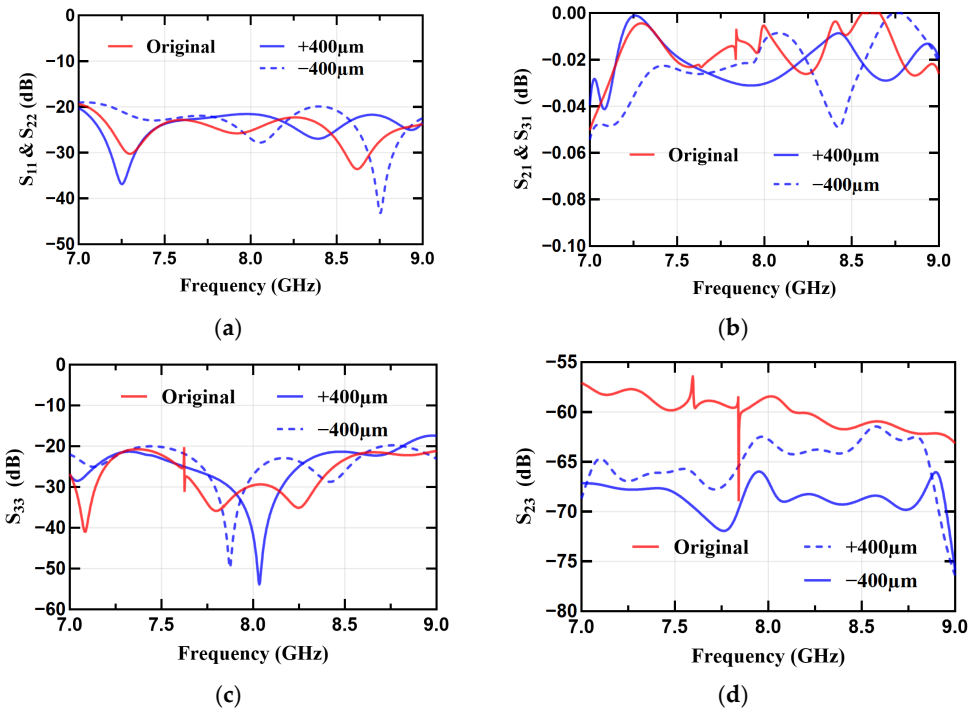


Figure 14. Tolerance analysis of the 400 μm design of different X−band OMT parameters. (**a**) S_{11} & S_{22} analysis; (**b**) S_{21} & S_{31} analysis; (**c**) S_{33} analysis; (**d**) S_{23} analysis.

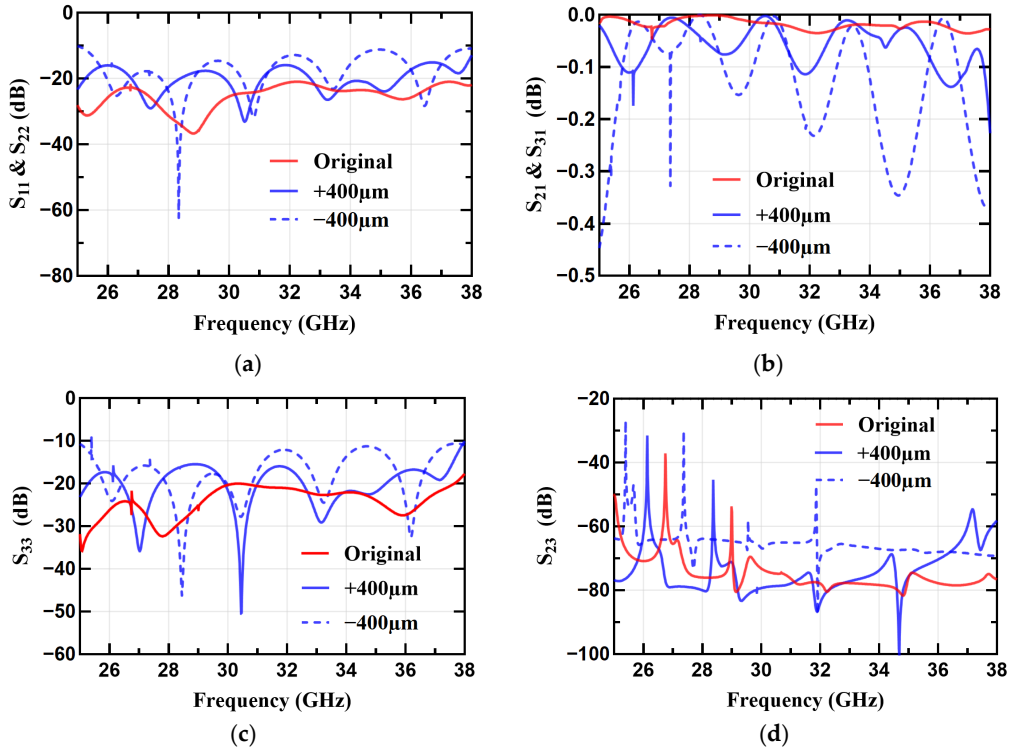


Figure 15. Tolerance analysis of the 400 μm design of different Ka-band OMT parameters. (**a**) S_{11} & S_{22} analysis; (**b**) S_{21} & S_{31} analysis; (**c**) S_{33} analysis; (**d**) S_{23} analysis.

4. Fabrication and Measurements

4.1. Fabrication

The proposed X-band OMT was fabricated using mask stereolithography (MSLA) technology with photocurable Formlabs Grey Pro Resin V4 (Formlabs, Somerville, MA, USA) as printing material. Subsequently, manual conductive painting was performed in-house at the UNSW laboratory. The printer used was a Phrozen Sonic XL 4K (Phrozen Tech Co., Ltd., Hsinchu City, Taiwan), with a print volume of 192 mm × 120 mm and an accuracy of 50 µm. The accuracy values refer to the general dimensional accuracy of the printed parts as specified by the 3D printer manufacturers, representing the standard tolerances of the processes. Due to the spatial limitations of the printer, the OMT structure was divided into four parts for 3D printing. These parts were designed to ensure that the rectangular waveguide network is symmetrically split along the E-plane, thereby minimizing loss and mismatch. Before printing, flanges and waveguide walls were incorporated into the model of the proposed OMT. The flange dimensions for the rectangular waveguide ports were selected based on the standard WR-112. The flange size for the circular waveguide port can be adjusted as needed. The prototypes were metallized with MG Chemicals 842AR silver conductive paint (MG Chemicals, Burlington, ON, Canada). The conductivity of the paint is approximately 1.3×10^6 S/m. The paint was applied manually in two successive coatings using a fine brush to ensure uniform coverage. Each layer was air-dried for 20 min, followed by a final curing stage at room temperature for 24 h. The resulting conductive film had an estimated thickness of 25–30 µm, corresponding to a measured surface resistance of approximately 0.03 Ω/sq. Figure 16 shows four different fabricated and painted OMT parts.

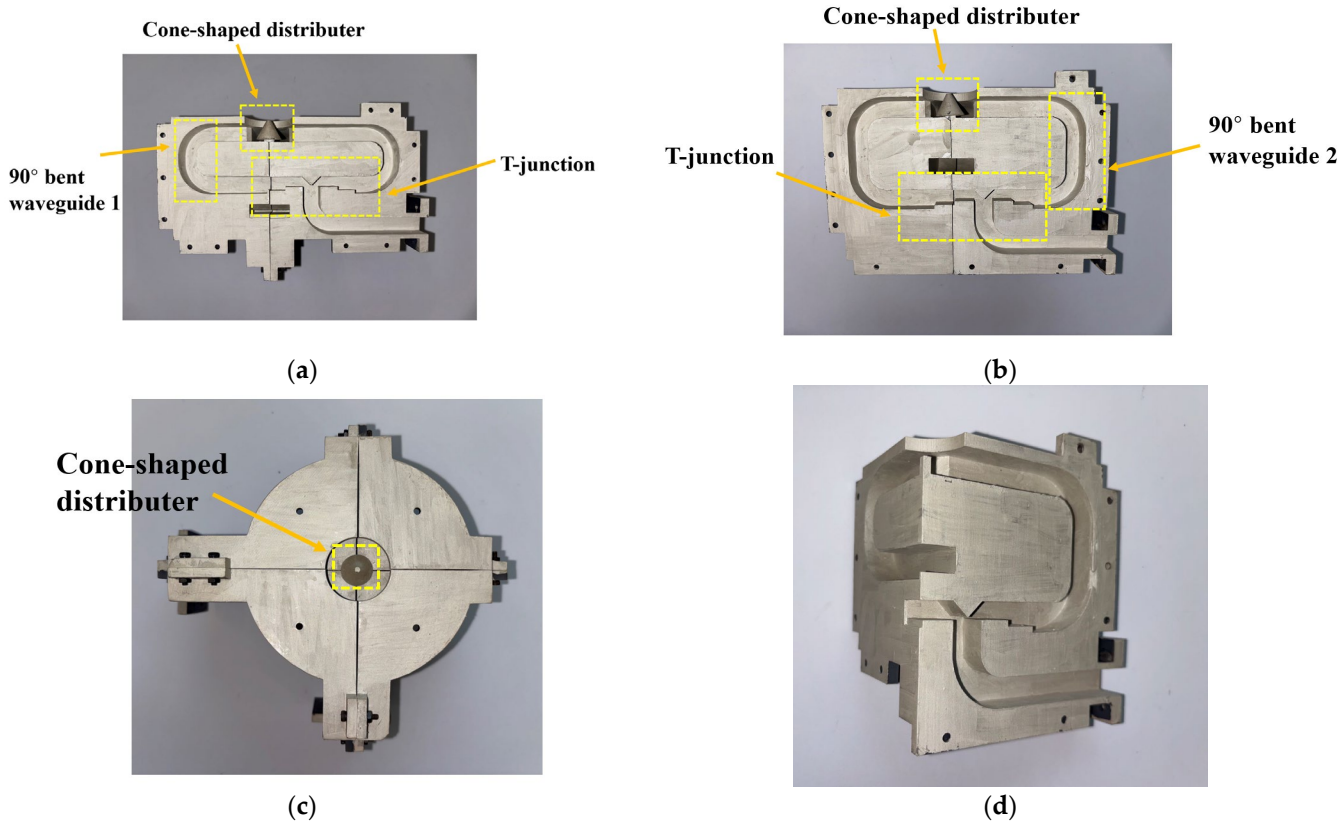


Figure 16. Fabricated prototypes of different parts of the X-band OMT. (**a**) Network 1; (**b**) network 2; (**c**) t op view; (**d**) one of the fabricated prototypes of OMT parts.

Figure 16a,b illustrate the different signal networks of the OMT. In Figure 16a,b, 90-degree bend waveguides connect the turnstile junction to the T-junction at the bottom. Waveguide bends of different lengths are used for different networks. Figure 16c provides a top view of the OMT, where the cone-shaped matching structure within the top turnstile junction ensures excellent matching at the circular waveguide port. Figure 16d displays one of the individually printed parts. Finally, after orthogonal separation, the two pairs of signals combine at the T-junctions and are output from ports 2 and 3, as shown in Figure 17. The complete OMT consists of three ports: port 1 is the circular waveguide port, while ports 2 and 3 are WR-28 rectangular waveguide ports. Figure 17 illustrates the assembled OMT.

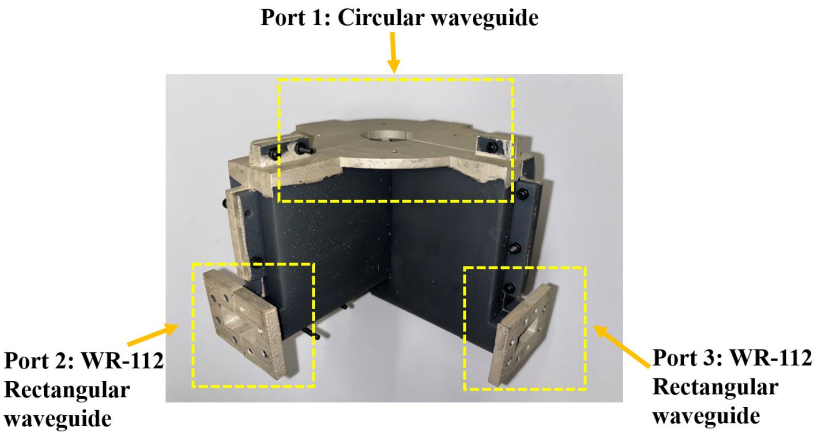


Figure 17. Fabricated and assembled X-band OMT prototype.

For the Ka band OMT, a comparative study was conducted to evaluate the performance of OMTs fabricated using different printing technologies, resulting in the production of three OMT prototypes, named OMT1, OMT2, and OMT3. The rectangular waveguide port uses the standard WR28 as the flange. The first prototype, OMT1, was fabricated using SLA technology with UTR Imagine Black resin as the printing material, followed by in-house manual silver conductive painting and copper electroplating. The Ka-band OMT features a compact and relatively complex internal structure, including a curved annular waveguide. During the 3D printing slicing process, internal supports are typically required to prevent bending or collapse of the internal structure. However, removing these supports post-printing is challenging due to their small size, potentially leaving residual structures or protrusions on the waveguide's inner surface. Such protrusions can compromise the smoothness of the printed component, significantly impacting the OMT's performance. To mitigate this issue, OMT1 was divided into four parts for 3D printing, with printing angles carefully adjusted to ensure that all support structures were located on the external shell of the OMT, avoiding internal surfaces. The second prototype, OMT2, was also fabricated using SLA technology but with UTR 3000 resin as the printing material. Similarly, OMT2 required electroplating for surface metallization. The third prototype, OMT3, was produced using SLM with AlSi10Mg as the printing material. The advantage of metal printing is that it eliminates the need for post-processing metallization, offering superior conductivity. However, the primary limitation is a reduced printing accuracy of approximately 300 μm. This accuracy value also refers to the standard tolerance of the printed parts provided by the additive manufacturing tool manufacturer. All three printing processes were completed by a commercial AM company.

For the SLA printed OMTs, metallization was further enhanced by applying an in-house copper electroplating step on top of the silver conductive paint layer, followed by the instruction in [28]. This process produced a uniform copper layer with a thickness of approximately 8–10 μm, confirmed using simultaneously plated calibration coupons.

According to the plating specifications, the conductivity of the electroplated copper is close to that of copper, which is about 5.8×10^7 S/m. Figure 18 shows different fabricated Ka-band OMT prototypes.

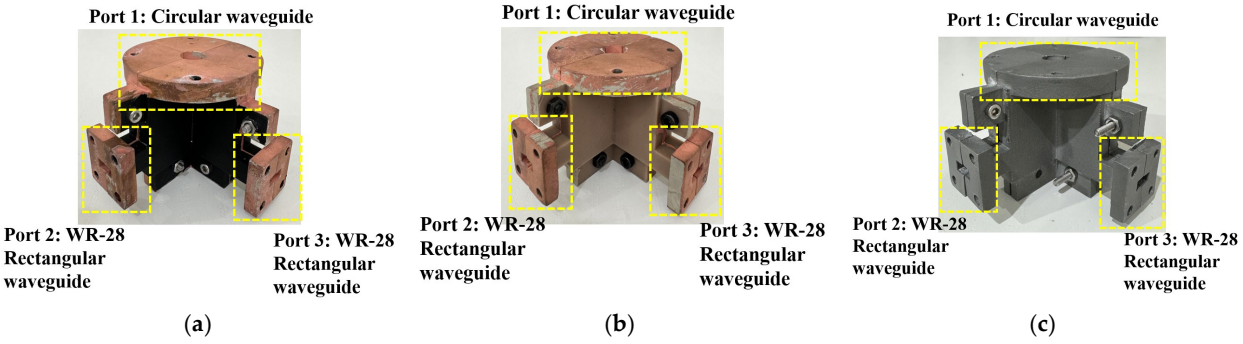


Figure 18. Different fabricated prototypes of Ka-band OMT. (**a**) SLA printed OMT1 with UTR Imagine Black resin; (**b**) SLA printed OMT2 with UTR 3000 resin; (**c**) SLM metal printed OMT3 with AlSi10Mg alloy.

4.2. Measurements

The S-parameters of the X-band OMT were measured using a VNA with a circular-to-rectangular waveguide adapter at the circular waveguide port. The measured results are presented in Figure 19. Across all three ports of the OMT, the return loss was below −15 dB, demonstrating excellent impedance matching. The average insertion losses measured between ports 1 and 2 and 3 were 1.6 dB and 2.1 dB, respectively. The elevated insertion loss is primarily attributed to poor connections and gaps between components and the relatively low conductivity of the silver conductive paint. The average isolation between ports 2 and 3 is over 35 dB, ensuring effective separation of the two input orthogonal signals without mutual interference. To further improve insertion loss, copper electroplating could be applied in future iterations to enhance the conductivity of the waveguide walls.

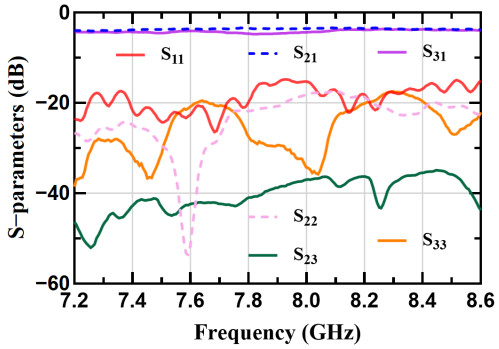


Figure 19. S-parameter measurement results of X-band OMT.

For the Ka-band OMT, the same measurement methodology as applied to the X-band OMT was used to evaluate the three OMT prototypes. The measurement results of OMT1, OMT2, and OMT3 are shown in Figures 20–22. The return loss at the circular waveguide port of OMT1 is below −13 dB, while the return losses at the other two ports are below −15 dB. The average insertion losses between the circular port and the two rectangular ports were 1.2 dB and 1.3 dB, respectively. The isolation between ports 2 and 3 was below −22 dB. For OMT2, due to manufacturing errors, the insertion loss in one of the transmission networks significantly increased, averaging 7.5 dB, rendering it unsuitable for use. Additionally, the average isolation between the two output ports was 30 dB. For OMT3, the return loss at both rectangular ports was below −15 dB, indicating acceptable

matching performance at each port. However, the return loss at the circular port was notably higher, approximately −13 dB. Owing to the inherent high conductivity of the metal, the insertion losses for the two transmission networks were approximately 2.1 dB and 2.4 dB, respectively. Furthermore, the average isolation between the two output ports was 30 dB, confirming the symmetry and orthogonal separation capability of the proposed OMT. The elevated return loss at the circular port is likely attributed to misalignment and gaps between the circular waveguide components.

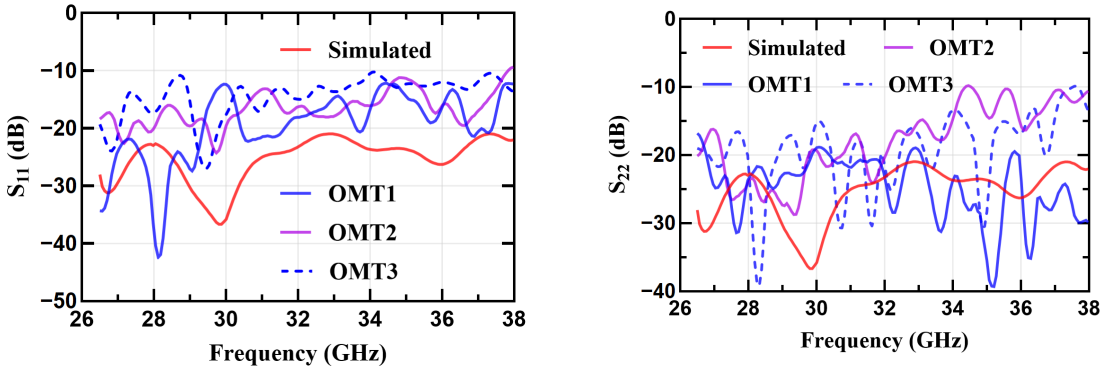


Figure 20. S-parameter measurement results of three Ka-band OMTs. (**a**) S_{11} measurement; (**b**) S_{22} measurement.

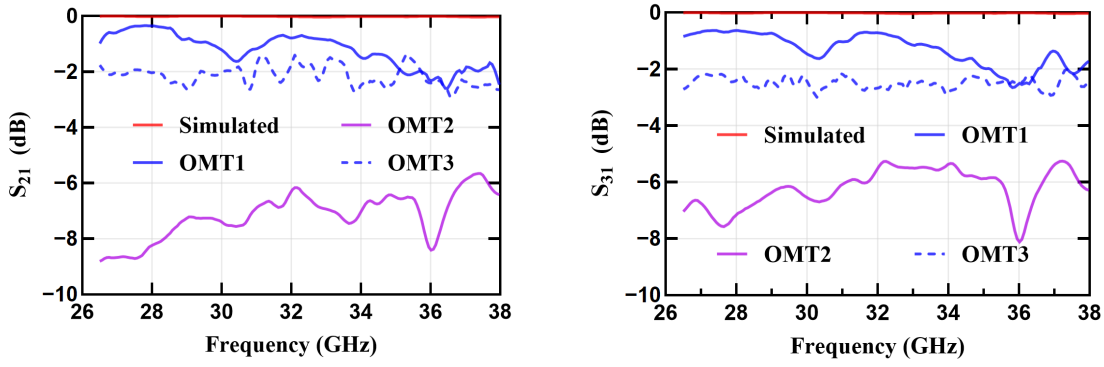


Figure 21. S-parameter measurement results of three Ka-band OMTs. (**a**) S_{21} measurement; (**b**) S_{31} measurement.

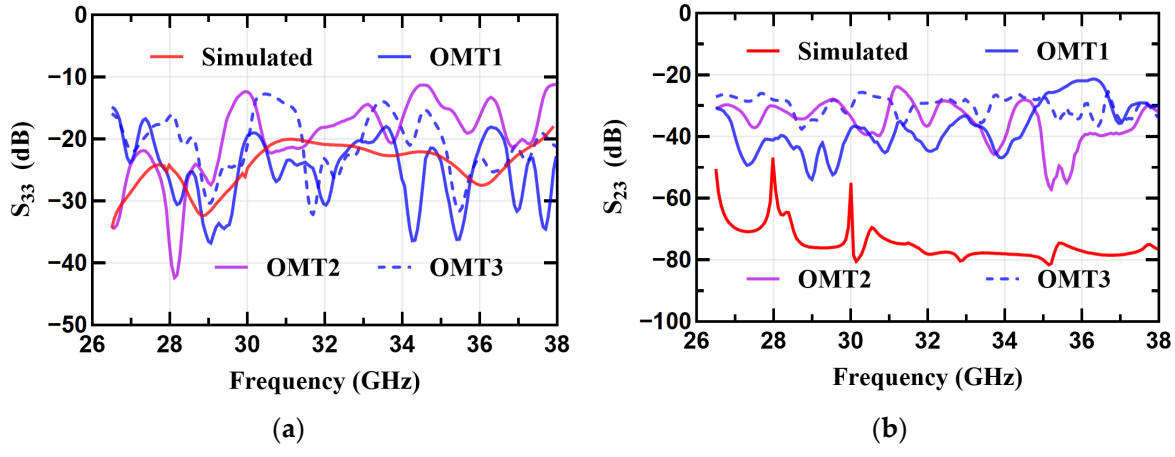


Figure 22. S-parameter measurement results of three Ka-band OMTs. (**a**) S_{33} measurement; (**b**) S_{23} measurement.

The measured results showed that high isolation could still be achieved, even in the presence of dimensional inaccuracies and assembly misalignments. This robustness can be attributed to the symmetry of the turnstile junction architecture. By exciting four arms arranged in quadrature, the structure enforces orthogonality between the two fundamental modes. As a result, small deviations in waveguide dimensions or moderate gaps at the flanges mainly affect impedance matching but have less influence on polarization purity. Therefore, the turnstile OMT design maintains decent polarization isolation as long as the overall symmetry of the junction is preserved.

Table 3 summarizes the measurement results and key specifications of the three OMT prototypes fabricated using different additive manufacturing technologies and materials. Overall, OMT1 exhibited the best performance among the three prototypes. The high precision of SLA effectively minimized uncertainties, while the UTR Imagine Black resin, once cured, resisted deformation, significantly reducing the size of any gaps during component assembly. This ensured lower insertion loss and higher return loss at each port. OMT2 is also fabricated using SLA technology. Due to fabrication-related imperfections, including dimensional deviations from the design values, surface roughness introduced during printing, and non-uniform coverage of the electroplated metallization layer, the effective conductivity of OMT2 was reduced. These imperfections significantly increased the insertion loss in one of the transmission networks, averaging 7.5 dB, rendering it unsuitable for use. In addition, the inferior performance of the OMT2 fabricated with UTR 3000 Resin can be attributed to its lower mechanical and thermal properties compared with UTR Imagine black Resin. Specifically, UTR 3000 Resin exhibits lower tensile and bending strength, reduced hardness, and a lower heat distortion temperature (46–50 °C). These limitations make it more prone to dimensional deformation during printing, curing, and assembly, leading to small geometric inaccuracies in the waveguide cross-sections. Additionally, its softer surface results in reduced metallization quality after conductive painting and electroplating, thereby increasing conductor losses. In contrast, UTR Imagine black Resin provides higher stiffness, hardness, and thermal stability (52–59 °C), which ensures better dimensional accuracy and smoother internal surfaces for metallization. Consequently, the OMT1 fabricated with UTR imagine black Resin demonstrated lower insertion loss, improved return loss, and more reliable polarization isolation than the prototype made with UTR 3000 Resin.

Table 3. Comparison between three fabricated OMTs.

Scope	OMT1	OMT2	OMT3
3D Printing Technology	SLA	SLA	SLM
Printing Material	UTR Imagine Black Resin	UTR 3000 Resin	AlSi10Mg metal Alloy
Cost (US Dollars)	17.25	17.26	106.07
Max. Return Loss (dB)	13	12.5	13
Average Insertion Loss (dB)	1.2, 1.3	7.5	2.1, 2.4
Isolation (dB)	Over 25 Average: 40	Over 22.5 Average: 30	Over 25 Average: 30
Avg. Dim. Error (Rect. waveguide)	0.15 mm	0.40 mm	0.20 mm
Avg. Dim. Error (Circ.waveguide)	0.06 mm	0.45 mm	0.35 mm

However, it should be noted that, due to the chosen printing technology and resin, other critical parameters remained highly reliable. OMT3, fabricated using SLM with metal material, provided excellent conductivity and mechanical rigidity but suffered from a tenfold reduction in printing accuracy, which substantially compromised the structural symmetry of the OMT, resulting in poorer isolation compared to the other two prototypes. Across all prototypes, the measured S-parameters began to degrade at frequencies above 35 GHz, primarily due to the propagation of higher-order modes in this frequency range, which diminished the overall performance of the OMT.

4.3. Dimensional Tolerances Analysis and RF Performance Discussion

To quantify the fabrication tolerances, multiple representative sections of both the rectangular and circular waveguide regions were selected from each OMT prototype. The fabricated dimensions were measured using precision calipers (resolution 0.01 mm) and compared with the original design values. The deviations obtained at different locations were averaged to calculate the mean dimensional error for each waveguide type. The results of these measurements are summarized in Table 3. The results show that OMT1, fabricated by SLA using UTR Imagine Black resin, achieved the highest dimensional accuracy (0.15 mm tolerance in rectangular and 0.06 mm tolerance in circular sections), which translated into low insertion loss and high isolation. OMT2 suffered from significantly larger dimensional deviations (0.40 mm and 0.45 mm tolerances), which prevented tight alignment at the circular port interface and resulted in excessive insertion loss. OMT3 benefited from superior conductivity due to the all-metal SLM process but exhibited larger dimensional errors (0.20 mm and 0.35 mm tolerances) because of the limited resolution of the process, compromising symmetry and degrading isolation. The results confirm that dimensional accuracy is a critical factor governing the RF performance of additively manufactured OMTs.

The performance difference between the X-band and Ka-band prototypes is mainly attributed to metallization and size effects. The Ka-band OMT employed a two-step process (silver conductive paint plus copper electroplating), while the X-band OMT used only silver paint. Since copper has more than an order of magnitude higher conductivity than the silver paint, the electroplated Ka-band prototype exhibited significantly lower ohmic loss. In addition, the larger size of the X-band OMT made it more susceptible to SLA fabrication distortions such as 1–3% volumetric shrinkage, uneven curing, residual stress, and warping. These errors accumulated into millimeter-scale dimensional mismatches and 2–3 mm assembly gaps, causing leakage and higher insertion loss.

5. Conclusions

This paper has presented turnstile-junction-based OMT prototypes developed using CST parametric sweeps and optimization tools. The X-band OMT, fabricated using SLA 3D printing with Formlabs Grey Pro Resin V4, achieved measured return losses below -15 dB, average insertion losses of 1.6–2.1 dB, and isolation above 35 dB. For the Ka-band, three prototypes were fabricated using SLA and SLM, with the OMT printed by SLA with UTR Imagine Black resin exhibiting superior performance, yielding insertion losses of 1.2–1.3 dB and isolation above 25 dB. Measurements validate AM's potential for producing micro-scale RF components, achieving a four-fold size reduction from X- to Ka-band while maintaining broadband operation. The results highlight the trade-offs between SLA's high precision and SLM's superior conductivity, providing critical insights into material and process optimization. Future research should focus on improving insertion loss through enhanced electroplating techniques, optimizing circular-to-rectangular waveguide transitions to reduce misalignment, and extending the design to higher-frequency bands for 5G/6G

applications. Integrating these OMTs with polarizers for axial ratio measurements and exploring hybrid AM techniques could further enhance performance, solidifying AM's role in next-generation RF micromachines for communication systems.

Author Contributions: Software, K.M.; Formal analysis, K.M.; Investigation, K.M.; Resources, X.W.; Writing—original draft, K.M.; Writing—review & editing, X.W., J.S.K. and R.R.; Visualization, R.R.; Supervision, J.S.K. and R.R.; Project administration, R.R.; Funding acquisition, R.R. All authors have read and agreed to the published version of the manuscript.

Funding: This research received no external funding.

Data Availability Statement: The original contributions presented in this study are included in the article. Further inquiries can be directed to the corresponding author.

Conflicts of Interest: The authors declare no conflict of interest.

References

1. Jin, H.; Huang, Y.M.; Jin, H.; Wu, K. E-Band Substrate Integrated Waveguide Orthomode Transducer Integrated with Dual-Polarized Horn Antenna. *IEEE Trans. Antennas Propag.* **2018**, *66*, 1515–1520. [CrossRef]
2. Shams, S.; Mahfouz, A.M.; Elsaadany, M.; Hassan, M.A.M.; Gagnon, G.; Kishk, A.A. Circularly Polarized V-Band Orthomode Transducer. *IEEE Antennas Wirel. Propag. Lett.* **2023**, *22*, 29–33. [CrossRef]
3. Fonseca, N.J.G. Very Compact Waveguide Orthomode Transducer in the K-Band for Broadband Communication Satellite Array Antennas. *Sensors* **2023**, *23*, 735. [CrossRef]
4. Zhao, Y.; Zhu, B.; Ding, J.; Li, S. A Whole W-Band Multi-Polarization Horn Antenna Based on Boifot-Type OMT. *Micromachines* **2024**, *15*, 385. [CrossRef] [PubMed]
5. Ding, C.; Meng, F.; Song, L. Design of a Ku-band Compact Dual Polarized Horn Arrays with OMT. In Proceedings of the 2018 IEEE MTT-S International Microwave Symposium (IMS), Philadelphia, PA, USA, 10–15 June 2018.
6. Singh, A.K.; Thakur, J.; Samminga, R.K. Design and Analysis of OMTs for Ku-Band. In Proceedings of the 6th International Conference for Convergence in Technology (I2CT), Maharashtra, India, 2–4 April 2021.
7. Navarrini, A.; Nesti, R. Characterization Techniques of Millimeter-Wave Orthomode Transducers (OMTs). *Electronics* **2021**, *10*, 1844. [CrossRef]
8. Tribak, A.; Cano, J.L.; Mediavilla, A.; Boussouis, M. Octave Bandwidth Compact Turnstile-Based Orthomode Transducer. *IEEE Microw. Wirel. Compon. Lett.* **2010**, *20*, 539–541. [CrossRef]
9. Fu, Y.; Chan, K.Y.; Ramer, R. Investigation of Orthogonal Modes in a Periodic Structure and Application to Two-Separate Beams Steering Within the Same Frequency Band. *IEEE Open J. Antennas Propag.* **2025**, *6*, 1096–1111. [CrossRef]
10. Fu, Y.; Gong, L.; Chan, K.Y.; Huang, S.; Nanzer, J.A.; Ramer, R. Design of a Compact Omnidirectional Leaky-Wave Antenna Fed by Higher Order Mode. *IEEE Trans. Antennas Propag.* **2022**, *70*, 1672–1682. [CrossRef]
11. Cheng, X.; Wang, Y.; Yao, Y.; Yu, T.; Yu, J.; Chen, X. Compact W-Band Septum Orthomode Transducer Based on Gap Waveguide. *IEEE Microw. Wirel. Technol. Lett.* **2023**, *33*, 133–136. [CrossRef]
12. Leal-Sevillano, C.A.; Reck, T.J.; Chattopadhyay, G.; Ruiz-Cruz, J.A.; Montejo-Garai, J.R.; Rebollar, J.M. Development of a Wideband Compact Orthomode Transducer for the 180–270 GHz Band. *IEEE Trans. Terahertz Sci. Technol.* **2014**, *4*, 634–636. [CrossRef]
13. Chen, S.; Li, J.; Xu, Z.; Yuan, T. A Ka-Band Wideband Monolithically Metallic 3-D Printed Turnstile Junction Orthomode Transducer with Shaped Internal Profile. In Proceedings of the 2022 IEEE/MTT-S International Microwave Symposium (IMS 2022), Denver, CO, USA, 19–24 June 2022; pp. 676–679.
14. Abdelaal, M.A.; Kishk, A.A. Ka-Band 3-D-Printed Wideband Groove Gap Waveguide Orthomode Transducer. *IEEE Trans. Microw. Theory Tech.* **2019**, *67*, 3361–3369. [CrossRef]
15. Coutts, G.M. Octave Bandwidth Orthomode Transducers for the Expanded Very Large Array. *IEEE Trans. Antennas Propag.* **2011**, *59*, 1910–1917. [CrossRef]
16. Shrestha, S.; Zahra, H.; Kiyani, A.; Asadnia, M.; Abbas, S.M.; Mahmoud, A. Miniaturized Wideband Antenna Prototype Operating over the Ku-Band. *Micromachines* **2022**, *13*, 471. [CrossRef] [PubMed]
17. Chin, S.Y.; Dikshit, V.; Meera Priyadarshini, B.; Zhang, Y. Powder-Based 3D Printing for the Fabrication of Device with Micro and Mesoscale Features. *Micromachines* **2020**, *11*, 658. [CrossRef] [PubMed]
18. Gao, B.; Zhao, H.; Peng, L.; Sun, Z. A Review of Research Progress in Selective Laser Melting (SLM). *Micromachines* **2023**, *14*, 57. [CrossRef] [PubMed]
19. Deng, T.; Chan, K.Y.; Fu, Y.; Ramer, R. An Analytical Design Method for a Wideband Differential Waveguide Directional Coupler With De-Embedding Analysis. *IEEE Trans. Instrum. Meas.* **2024**, *73*, 1–9. [CrossRef]

20. Li, L.; Lan, D.; Han, X.; Liu, T.; Dewdney, J.; Zaman, A.; Guneroglu, U.; Martinez, C.M.; Wang, J. Low Phase Noise, Dual-Frequency Pierce MEMS Oscillators with Direct Print Additively Manufactured Amplifier Circuits. *Micromachines* **2025**, *16*, 755. [CrossRef]
21. Fu, Y.; Chan, K.Y.; Bozzi, M.; Ramer, R. 3-D-Printed Monolithically Integrated Waveguide Polarizer. *IEEE Trans. Microw. Theory Tech.* **2025**, *73*, 5696–5710. [CrossRef]
22. Sorocki, J.; Piekarz, I.; Baranowski, M.; Lamecki, A.; Cattenone, A.; Marconi, S.; Alaimo, G.; Delmonte, N.; Silvestri, L.; Bozzi, M. Low-Cost Method for Internal Surface Roughness Reduction of Additively Manufactured All-Metal Waveguide Components. *IEEE Trans. Microw. Theory Tech.* **2024**, *72*, 4519–4529. [CrossRef]
23. Golhin, A.P.; Tonello, R.; Frisvad, J.R.; Grammatikos, S.; Strandlie, A. Surface Roughness of As-Printed Polymers: A Comprehensive Review. *Int. J. Adv. Manuf. Technol.* **2023**, *127*, 987–1043. [CrossRef]
24. Shen, J.; Ricketts, D.S. Compact W-Band "Swan Neck" Turnstile Junction Orthomode Transducer Implemented by 3-D Printing. *IEEE Trans. Microw. Theory Tech.* **2020**, *68*, 3408–3417. [CrossRef]
25. Henke, D.; Claude, S. Design of a 70–116 GHz W-Band Turnstile OMT. In Proceedings of the 44th European Microwave Conference, Rome, Italy, 6–9 October 2014; pp. 456–459.
26. Zhang, J.; He, Y.; Huang, T.; Zhang, W.; Zhao, Y.; Wang, W.; Zhang, Y. 170–260-GHz Ultrawideband and High Isolation Orthomode Transducer Based on Symmetric Reverse Coupling Structure. *IEEE Trans. Microw. Theory Techn.* **2023**, *71*, 2169–2177. [CrossRef]
27. Pisano, G.; Savini, G.; Ade, P.A.R.; Haynes, V. A Broadband WR10 Turnstile Junction Orthomode Transducer. *IEEE Microw. Wirel. Compon. Lett.* **2007**, *17*, 286–288. [CrossRef]
28. Tamayo-Dominguez, A.; Sanchez-Olivares, P.; Camacho-Hernandez, A.; Fernandez-Gonzalez, J.-M. Guidelines for Accurate In-House Electroplating and 3-D-Printing Processes Applied to mm-Wave Devices. *IEEE Microw. Wirel. Compon. Lett.* **2022**, *32*, 1267–1270. [CrossRef]

Disclaimer/Publisher's Note: The statements, opinions and data contained in all publications are solely those of the individual author(s) and contributor(s) and not of MDPI and/or the editor(s). MDPI and/or the editor(s) disclaim responsibility for any injury to people or property resulting from any ideas, methods, instructions or products referred to in the content.